33. D. B. Campbell, D. A. Senske, J. W. Head, A. A. Hine, P. C. Fisher, *Science* **251**, 180 (1991).
34. M. T. Zuber, *Geophys. Res. Lett.* **17**, 1369 (1990).
35. V. P. Kryuchkov, *Lunar Planet. Sci.* **19**, 649 (1988).
36. A. L. Sukhanov and A. A. Pronin, *Proc. 19th Lunar Planet. Sci. Conf.* (1989), p. 335.
37. J. W. Head, *J. Geophys. Res.* **95**, 7119 (1990).
38. D. L. Bindschadler and J. W. Head, *J. Geophys. Res.*, in press.
39. BVSP (Basaltic Volcanism Study Project), *Basaltic Volcanism on the Terrestrial Planets* (Pergamon, New York, 1981).
40. Yu. A. Surkov, *Proc. 8th Lunar Sci. Conf.* (1977), p. 2665.
41. Yu. A. Surkov *et al.*, *Proc. 17th Lunar Planet. Sci. Conf., J. Geophys. Res.* **92**, E537 (1987).
42. J. H. Hoffman, R. R. Hodges, T. M. Donahue, M. B. McElroy, *J. Geophys. Res.* **85**, 7882 (1980).
43. T. M. Donahue and J. B. Pollack, in *Venus*, D. M. Hunten, L. Colin, T. M. Donahue, V. I. Moroz, Eds. (Univ. of Arizona Press, Tucson, 1983), pp. 1003–1036.
44. D. L. Turcotte and K. Burke, *Earth Planet. Sci. Lett.* **41**, 341 (1978).
45. D. McKenzie and F. M. Richter, *J. Geophys. Res.* **86**, 11,667 (1981).
46. J. Arkani-Hamed and M. N. Toksöz, *Phys. Earth Planet. Inter.* **34**, 232 (1984); N. H. Sleep, M. A. Richards, B. H. Hager, *J. Geophys. Res.* **93**, 7672 (1988).
47. V. S. Solomatov and V. N. Zharkov, *Icarus* **84**, 280 (1990).
48. M. K. McNutt, *J. Geophys. Res.* **89**, 11,180 (1984).
49. S. C. Solomon and J. W. Head, *Lunar Planet. Sci.* **21**, 1180 (1990).
50. ———, *Geophys. Res. Lett.* **17**, 1393 (1990).
51. D. L. Turcotte, *J. Geophys. Res.* **94**, 2779 (1989).
52. A. T. Basilevsky *et al.*, *ibid.* **92**, 12,869 (1987).
53. R. E. Grimm and S. C. Solomon, *Geophys. Res. Lett.* **14**, 538 (1987).
54. R. E. Arvidson, R. E. Grimm, R. J. Phillips, G. G. Schaber, E. M. Shoemaker, *ibid.* **17**, 1385 (1990).
55. B. Fegley, Jr., and R. G. Prinn, *Nature* **337**, 55 (1989).
56. J. A. Wood and A. Hashimoto, *Lunar Planet. Sci.* **22**, 1519 (1991).
57. R. J. Phillips and M. C. Malin, in *Venus*, D. M. Hunten, L. Colin, T. M. Donahue, V. I. Moroz, Eds. (Univ. of Arizona Press, Tucson, 1983), pp. 159–214.
58. P. Morgan and R. J. Phillips, *J. Geophys. Res.* **88**, 8305 (1983).
59. R. E. Grimm and S. C. Solomon, *ibid.* **94**, 12,103 (1989).
60. D. J. Stevenson, T. Spohn, G. Schubert, *Icarus* **54**, 466 (1983).
61. J. F. Schatz and G. Simmons, *J. Geophys. Res.* 77, 6966 (1972).
62. B. Parsons and J. G. Sclater, *ibid.* **82**, 803 (1977).
63. W. S. Kiefer, M. A. Richards, B. H. Hager, B. G. Bills, *Geophys. Res. Lett.* **13**, 14 (1986).
64. M. T. Zuber, *Proc. 17th Lunar Planet. Sci. Conf., J. Geophys. Res.* **92**, E541 (1987); M. T. Zuber and E. M. Parmentier, *Icarus* **85**, 290 (1990).
65. R. E. Grimm and S. C. Solomon, *J. Geophys. Res.* **93**, 11,911 (1988).
66. S. R. Taylor, *Tectonophysics* **161**, 147 (1989).
67. Yu. A. Surkov, V. L. Barsukov, L. P. Moskalyeva, V. P. Kharyukova, A. L. Kemurdzhian, *Proc. 14th Lunar Planet. Sci. Conf., J. Geophys. Res.* **89**, B393 (1984).
68. P. C. Hess and J. W. Head, *Earth Moon Planets* **50/51**, 57 (1990).
69. D. L. Anderson, *Geophys. Res. Lett.* 7, 101 (1980).
70. W. M. Kaula, *Lunar Planet. Sci.* **19**, 593 (1988).
71. W. B. Banerdt and M. P. Golombek, *J. Geophys. Res.* **93**, 4759 (1988).
72. J. W. Head, *Earth Moon Planets* **50/51**, 5 (1990).
73. J. A. Crisp, *J. Volcanol. Geotherm. Res.* **20**, 177 (1984).
74. R. White and D. McKenzie, *J. Geophys. Res.* **94**, 7685 (1989).
75. D. McKenzie and M. J. Bickle, *J. Petrol.* **29**, 625 (1988).
76. D. R. Scott and D. J. Stevenson, *J. Geophys. Res.* **94**, 2973 (1989).
77. C. Sotin, D. A. Senske, J. W. Head, E. M. Parmentier, *Earth Planet. Sci. Lett.* **95**, 321 (1989).
78. R. J. Phillips, R. E. Grimm, M. C. Malin, *Science* **252**, 288 (1991).
79. P. J. McGovern and S. C. Solomon, *Lunar Planet. Sci.* **20**, 669 (1989).
80. W. M. Kaula, *Science* **247**, 1191 (1990).
81. R. J. Phillips, *J. Geophys. Res.* **95**, 1301 (1990).
82. E. M. Robinson, B. Parsons, S. F. Daly, *Earth Planet. Sci. Lett.* **82**, 335 (1987).
83. R. J. Phillips, *Geophys. Res. Lett.* **13**, 1141 (1986).
84. D. Bercovici, G. Schubert, G. A. Glatzmaier, *Science* **244**, 950 (1989).
85. G. Schubert, D. Bercovici, G. A. Glatzmaier, *J. Geophys. Res.* **95**, 14,105 (1990).
86. B. Parsons and S. Daly, *ibid.* **88**, 1129 (1983).
87. M. A. Richards, R. A. Duncan, V. E. Courtillot, *Science* **246**, 103 (1989).
88. R. R. Herrick and R. J. Phillips, *Geophys. Res. Lett.* 17, 2129 (1990).
89. S. E. Smrekar and R. J. Phillips, *ibid.* **15**, 693 (1988).
90. W. S. Kiefer and B. H. Hager, *Lunar Planet. Sci.* **20**, 520 (1989); D. L. Bindschadler, G. Schubert, W. M. Kaula, *Geophys. Res. Lett.* **17**, 1345 (1990).
91. A. A. Pronin, *Geotectonics* **20**, 271 (1986); A. T. Basilevsky, *ibid.*, p. 282.
92. R. E. Grimm and R. J. Phillips, *Geophys. Res. Lett.* **17**, 1349 (1990).
93. S. P. Clark, Jr., in *Handbook of Physical Constants, Memoir 97*, S. P. Clark, Ed. (Geological Society of America, Boulder, CO, 1966) pp. 459–482.
94. D. R. Williams and V. Pan, *Geophys. Res. Lett.* **17**, 1397 (1990).
95. We thank D. McKenzie for performing the calculations depicted in Fig. 4, and W. M. Kaula, G. G. Schaber, and N. H. Sleep for helpful comments on an earlier draft. S.C.S. was a Visiting Associate in the Division of Geological and Planetary Sciences, California Institute of Technology, during the writing of this manuscript. This research was supported by the National Aeronautics and Space Administration under contracts 957070 and 957088 from the Jet Propulsion Laboratory and grants NAGW-1937 and NAGW-713.

8 January 1991; accepted 25 February 1991

Magellan: Radar Performance and Data Products

GORDON H. PETTENGILL, PETER G. FORD, WILLIAM T. K. JOHNSON, R. KEITH RANEY, LAURENCE A. SODERBLOM

The Magellan Venus orbiter carries only one scientific instrument: a 12.6-centimeter-wavelength radar system shared among three data-taking modes. The synthetic-aperture mode images radar echoes from the Venus surface at a resolution of between 120 and 300 meters, depending on spacecraft altitude. In the altimetric mode, relative height measurement accuracies may approach 5 meters, depending on the terrain's roughness, although orbital uncertainties place a floor of about 50 meters on the absolute uncertainty. In areas of extremely rough topography, accuracy is limited by the inherent line-of-sight radar resolution of about 88 meters. The maximum elevation observed to date, corresponding to a planetary radius of 6062 kilometers, lies within Maxwell Mons. When used as a thermal emission radiometer, the system can determine surface emissivities to an absolute accuracy of about 0.02. Mosaicked and archival digital data products will be released in compact disk (CDROM) format.

MAGELLAN'S RADIO AND RADAR observations of Venus involve three distinct modes of operation: (i) side-looking synthetic aperture (SAR) imaging, (ii) nadir-directed altimetry, and (iii) thermal emission radiometry. The observations are carried out with a common radar instrument comprising eight units that are completely duplicated onboard to provide double-string operational redundancy. (As of the end of December 1990, there have been no failures in the radar, and all units are still drawn only from the prime system.) The performance of the radar in each of these time-shared modes is detailed in separate sections below.

The design of the Magellan radar system reflects the mission's scientific objectives, which include the imaging of more than 70% of the surface of Venus at a resolution of better than 360 m and a determination of a corresponding part of the planet's topography with a height resolution commensurate with the imaging waveform. The radar system as implemented can image about 90% of the surface during the first 8 months of the mission, and more than half of that is at a resolution of better than 130 m. It should eventually be able to map the entire planetary surface, using data obtained in additional mapping cycles extending beyond the first 8 months of operation.

The transmitter, receiver, waveform generator, and timing systems (Table 1) are shared among the three operating modes. In the two radar modes, the transmitter employs a pulse consisting of 60 elements of a biphase code that has been carefully chosen to minimize time-delay sidelobes. By the use of an amplitude-tapered decoding (compression) sequence, the point-spread func-

G. H. Pettengill and P. G. Ford, Massachusetts Institute of Technology, Cambridge, MA 02139.
W. T. K. Johnson, Jet Propulsion Laboratory, California Institute of Technology, Pasadena, CA 91109.
R. Keith Raney, Canada Centre for Remote Sensing, Ottawa, Ontario K1A 0Y7, Canada.
L. A. Soderblom, U.S. Geological Survey, Flagstaff, AZ 86001.

Table 1. Magellan radar characteristics; T, temperature.

Parameter	Value
Radar operating frequency	2.385 GHz
Radar wavelength	12.6 cm
Transmitter peak power	400 W
Receiving system T (on Venus)	1250 K
SAR 3.7-m parabolic antenna: gain	36.0 dB
: angular beamwidth	2.1° by 2.5°
Altimeter horn antenna: gain	19.0 dB
: angular beamwidth	10° by 30°
Modulation bandwidth	2.26 MHz
Transmitted pulse length	26.5 μs
Time-bandwidth product	60
Effective slant-range resolution	0.59 μs (88 m)
Along-track (Doppler) resolution	120 m

Table 2. SAR characteristics versus spacecraft altitude.

Altitude (km)	Latitude (degrees)	Incidence angle (degrees)	Range resolution (m)	Azimuth resolution (m)	Looks
290	+10	47	120	120	5
400	+23, −3	43	130	120	6
600	+46, −26	37	135	120	7
1000	+62, −42	29	175	120	10
1750	+83, −63	19	250	120	15
2100	+90, −67	17	280	120	17

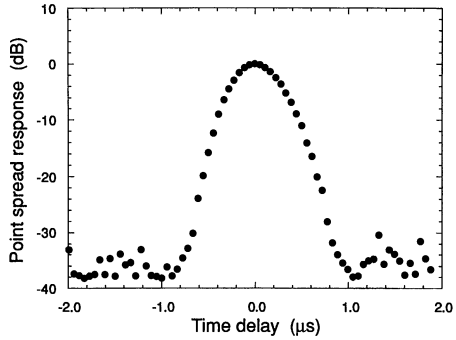

Fig. 1. Delay response (point-spread function) of the Magellan radar system to an echo from a point target.

tion (*1*) that results is extremely clean along the time axis, as seen from prelaunch test data (Fig. 1). The largest sidelobe value found anywhere on the time axis is 26 dB below the peak.

In operation, the radar system is connected either to the 3.7-m-diameter parabolic high-gain antenna (HGA), when carrying out SAR imaging or thermal radiometry, or to a smaller nadir-directed horn antenna (Table 1), when making altimetric observations. The large paraboloid is shared with the spacecraft's telemetry system, where it is used to transmit the stored radar data back to Earth, following a radar mapping pass. Both antennas are fixed to the vehicle's structure, so that aiming them requires orienting the entire spacecraft. The radar system is sequenced among the three modes of operation, typically several times a second (Figs. 2 and 3).

In the SAR mode, with the radar connected to the HGA, the angle between the incident radar energy and the surface normal (the incidence angle) is varied as listed in Table 2 in order to maintain an acceptably high ratio of signal to noise against changes in the altitude of the spacecraft. Decreasing the angle of incidence increases the returned power and thus compensates for the increasing signal loss as the distance to the surface increases. As a consequence, the cross-track, or range, resolution also varies; however, the duration of the SAR burst (the coherence interval that determines the synthetic aperture) is increased with altitude to maintain a constant resolution in the along-track, or azimuth, direction. The number of successive bursts (called "looks") within which a given point on the surface remains illuminated by the antenna's main lobe also varies with altitude. The more looks there are, the better the statistical accuracy with which the surface echoing intensity is determined, and thus the easier the task of distinguishing adjacent areas having slightly different echoing properties (*2*).

The echo samples obtained during a SAR burst are digitized and recorded on magnetic tape during the (nominally 37-min) duration of a radar pass. They are later telemetered to Earth and processed into image strips. These strips, when projected to the Venus surface with the use of a model for surface altitudes constructed from observations made by earlier spacecraft missions, constitute the primary data product of the Magellan mission. They represent the imaged swath from a single pass, and are typically about 20 km wide by some 15,000 km long. The image elements, or pixels, are specified at intervals of 75 m, and have numeric values interpretable as the dimensionless scattering efficiency of the surface, that is, the specific radar cross section. The pixel values have an absolute accuracy of about a factor of 2, whereas the relative accuracy among pixels in a given swath is about 25%.

The raw-image strips are digitally assembled into a series of full-resolution mosaics (called F-MIDRs) that each cover an area roughly 530 km (5° of latitude) square. It would require some 1650 of these to image the entire planet, but only 220 (selected to cover the most geologically interesting regions) will be prepared immediately, in order to hold down project expenses. The entire planet, however, will be displayed at a threefold coarser resolution, requiring a total of 179 approximately 1600-km-square mosaics (called C1-MIDRs) whose pixels, spaced at 225 m, have been obtained by averaging over a 3 by 3 block of full-resolution data. The averaging process increases the effective number of looks by a factor of between 2 and 4 (depending on the original imaging resolution) and reduces the statistical fluctuations in the intensity of the data (called "speckle") by a factor of as much as 2; as a result, the discernible contrast between adjoining surface features is significantly improved. Two other series of images (*3*), coarsened by a further factor of 3 (the C2-MIDR) and 9 (the C3-MIDR), respectively, from the C1-MIDRs (Table 3), will allow better contextual interpretation of

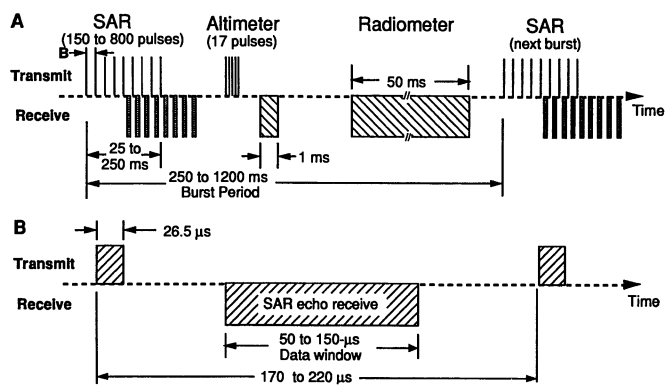

Fig. 2. (**A**) Radar-burst time line, showing detailed assignment to the three operating modes. (**B**) Detail of the interval between transmitted SAR pulses.

Table 3. Magellan data products; N/A, not applicable.

Acronym	Volume*	Pixel spacing (km)	Description
F-MIDR	220	0.075	Full resolution SAR mosaic
C1-MIDR	179	0.225	Compressed-once SAR mosaic
C2-MIDR	26	0.675	Compressed-twice SAR mosaic
C3-MIDR	6	2.025	Compressed-thrice SAR mosaic
ARCDR	30	N/A	Altimeter-radiometer database
GTDR	1	5.0	Global topography image
GSDR	1	5.0	Global rms-slope image
GREDR	1	5.0	Global Fresnel-reflectivity image
GEDR	1	5.0	Global emissivity image

*Refers to the number of complete data products to be produced during the nominal 8-month mission.

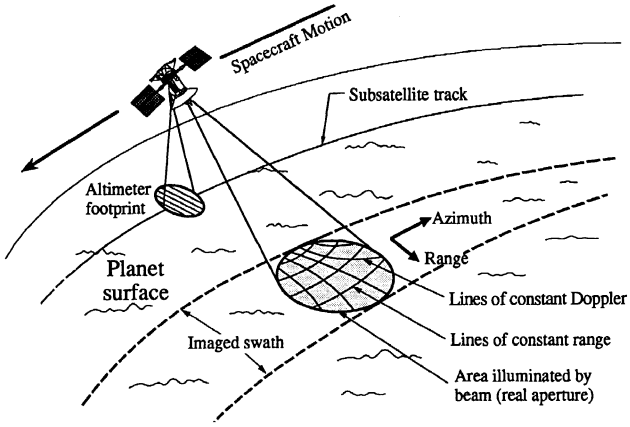

Fig. 3. Observing geometry for the Magellan SAR, altimetry, and radiometry modes of operation. Resolution of the surface across the swath tracks is obtained from the delay coordinate, whereas resolution along track comes from Doppler frequency analysis. In the radiometer mode, resolution is determined solely by the high-gain antenna pattern.

large features, as well as a global geological overview.

The power scattered back to a radar by the average Venus surface varies dramatically as the viewing angle changes (Fig. 4). Close to normal incidence (small angles), most of the scattered energy comes from small, radar-smooth facets inclined to the mean surface so that they are perpendicular to the viewing direction, and thus appear as preferentially "picked out" glints (*4*). In this regime, which typically dominates for viewing angles up to about 20°, the visual modulation seen in an image is largely controlled by variations in the local slopes across the viewed terrain. Examples of this phenomenon are particularly striking in areas containing a large number of small volcanic domes (*5*).

At angles of incidence above 25° or so, few facets of sufficient size are normally found with the corresponding steep inclination; echoes seen at large angles of incidence result primarily from diffuse scattering by surface roughness having structure sizes comparable to the radar wavelength (*6*). In this regime, changes in image intensity primarily signify varying densities of wavelength-sized scatterers on or near the surface (*7*). Scattering strengths seen in both regimes also depend on the bulk dielectric properties of the surface, of course.

In addition to modulating the backscattering efficiency, sloping terrain that faces toward or away from the direction of observation can distort the appearance of a surface feature, as compared to a true overhead plan view. This geometric distortion arises in the course of projecting the measured distribution of echo power in (slant-range) time delay on to the planetary figure, where the image processor must know the precise altitude of every element of the surface viewed, in order to calculate by trigonometry the corresponding surface coordinates. For small features, the topographic profile is not usually well known, at least in advance of the first observations, and a constant surface radius is therefore taken as an approximation. As a result, terrain sloping toward the radar is compressed in range as compared to level areas, whereas terrain sloping away is distended (Fig. 5). The effect is most severe at small angles of incidence, and is one of the reasons that as large an angle of incidence as possible has been used in initial radar surveys (such as the Magellan nominal mission). In extreme cases, a slope may exceed the angle of incidence, pass through right angles to the line of sight, and actually turn over in its mapped projection such that the bottom of the slope is projected as lying farther from the viewing radar than the top. This situation occurs often in mountainous areas viewed at low angles of incidence and is called "layover." It greatly complicates the geometric interpretation of a radar map, but its presence is in some cases signaled by a characteristic bright crescent adjacent to a feature that is assumed to be inherently circular in planform (like a volcanic cone or impact crater).

In the altimetric mode (Fig. 2), the radar system is connected to the altimeter horn antenna, and a 1.1-ms burst containing 17 pulses is transmitted. After a programmed delay that allows for the changing spacecraft altitude, a 1-ms receiving interval is sampled. The transmitting interval is slightly longer than the receiving interval, in order to ensure that the echo data completely fill the sampled region despite small uncertainties in the spacecraft orbit or terrain height. Because the minimum spacecraft altitude (periapsis) is about 290 km, corresponding to a round-trip echo delay of 1.94 ms, the transmitted burst is always finished well before reception begins.

Although fixed to the spacecraft at an offset of 25° with respect to the axis of the HGA, the horn-antenna pattern is sufficiently broad in the across-track direction (30°) that it can view the nadir without serious loss in signal strength even while the spacecraft is aiming the HGA to achieve SAR incidence angles other than 25° (Table 2). In the along-track direction, the pattern is narrow (10°), so that the altimeter's observations largely avoid unwanted delay and frequency aliasing (*8*).

The data values from each altimeter burst, corresponding to echoes from 15 transmitted pulses, are telemetered back to Earth, where they are processed by separate groups in three distinct ways: (i) time compression with the same point-spread response as in Fig. 1, followed by detection of the rising edge of the first threshold-crossing nadir echo; (ii) time compression as in (i), followed by frequency filtering, multi-burst summation, and model-dependent analysis to achieve simultaneous estimates of surface height, meter-scale roughness, and normal-incidence power reflection coefficient; and (iii) direct inversion of the delay and frequency spectra to derive a model-independent measure of the radar scattering function but no estimate of surface heights. Method (i) is carried out at the Jet Propulsion Laboratory, Pasadena, California, (*9*), and is intended primarily for "quick-look" analysis. Method (iii) is undertaken at Stanford University, Stanford, California, and is discussed elsewhere (*10*). The discussion below is confined to method (ii), which is carried out at the Massachusetts Institute of Technology, Cambridge, Massachusetts.

The dimensions of the area resolved by the Magellan altimeter on the Venus surface (called a "footprint") depend primarily on the time and frequency characteristics of the

radar signal, somewhat on the topographic relief encountered, and not at all on the beamwidth of the horn antenna. Because the altimeter receiving interval is only 1 ms long, as compared to 25 to 250 ms in the SAR mode, the along-track Doppler resolution varies from 2 km (*11*) at periapsis to 20 km at high altitudes in the north polar region (Table 4). The across-track resolution is governed by the point-spread time responses, as well as the topography, and varies from 13 km at periapsis to 31 km at the north pole.

Echo components originating in footprints located ahead of, or behind, the instantaneous spacecraft nadir will be Doppler-shifted to higher or lower frequencies, respectively, as indicated in Fig. 3. For a given footprint, components at frequencies other than that of nadir have been obtained at incidence angles whose tangents are proportional to their frequency separation from nadir. They have thus traveled over a geometrically calculable longer path (when corrected for intervening spacecraft motion) than echoes from nadir. After time compression and frequency filtering, data from separate altimeter bursts are sorted according to the surface footprint from which they come, and the data corresponding to a given footprint are combined in two separate ways.

In the first method, each frequency-resolved, time-delay echo profile corresponding to a given Doppler offset from nadir is slid earlier in time delay by an amount corresponding to the additional geometric delay for that viewing angle; the sequences of different-frequency data for a given footprint are then summed together. In this way, a composite ("range-sharpened") delay profile is synthesized that maximizes the sharpness of the surface-echo response and optimizes estimation of the distance of that footprint from the spacecraft. Knowledge of the orbital position of the spacecraft allows conversion of this distance to a surface height. In the second method, data from different frequencies are added together without a geometrical delay correction. The latter ("range-unsharpened") product retains the sensitivity of the delay profile to the angular scattering law, and optimizes estimation of meter-scale surface slopes. Both profiles contain information on the total scattering strength.

Analysis of the delay to, and shape of, the two kinds of echo profiles can, therefore, yield estimates of three independent surface properties for a given footprint: (i) from the time of arrival of the echo, the range to the nadir is derived; (ii) from the total power detected in an echo profile, the power reflection coefficient of the surface is obtained; and (iii) from the shape of the trailing edge

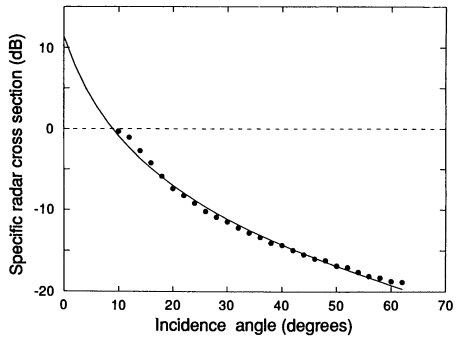

Fig. 4. The median-specific backscattered radar cross section for Venus versus angle of incidence, as obtained from Pioneer Venus (PV) observations (*6*) at a wavelength of 17 cm. The solid curve represents Muhleman's law (*15*), with parameters adjusted to optimize its fit to the PV data.

of the echo, the behavior of the scattering cross section versus the incidence angle is determined. The scattering behavior is, in turn, related to the meter-scale roughness of the surface (*4*). Because the relatively poor statistics associated with the limited number of looks available (Table 4) prevent an inversion of the echo profiles to obtain these parameters directly, a model-dependent approach is adopted that compares the echo profiles against a suite of precomputed "templates" representing the shape of the echo for particular values of spacecraft altitude and surface roughness.

The altimetric data are combined orbit by orbit with the spacecraft ephemerides and with data from the radiometric mode (described below) to form a product called the Altimetry and Radiometry Composite Data Record (ARCDR). Along with the surface properties derived for each altimetry footprint, this data set also contains both types of composite echo profiles and thus facilitates subsequent reanalysis of the altimetry with the use of other scattering models. In addition to the primary ARCDR data product, digital maps resampled to a uniform global grid will present topography (Global Topographic Data Record or GTDR), surface slope (GSDR), and power reflection coefficient (GREDR), as listed in Table 3.

Figure 6 shows a map of Venus topography as derived from the first 301 Magellan orbits, stretching nearly from pole to pole (the nadir-looking altimeter, of course, cannot map above northern, nor below southern, culmination, which is restricted to ±85.4° by the orbital inclination of Magellan), and spanning some 60° of longitude from the start of mapping on 15 September 1990, through the beginning of the superior conjunction mapping pause on 26 October 1990. The theoretical height accuracy of the altimeter over relatively smooth terrain is of

Table 4. Altimeter surface footprint characteristics versus spacecraft altitude. Resolution is given in kilometers; the two numbers in the last column refer to the sharpened and unsharpened modes, respectively (see text).

Spacecraft height (km)	Resolution		Looks
	Along track	Across track	
290	10	12	28/37
500	7	16	15/21
1500	12	25	25/53
2200	20	29	36/78

the order of 5 m, but uncertainties in determining the spacecraft orbit contribute an additional, slowly varying error on the order of 50 m. The surface roughness for this group of orbits is presented in (*10*), and analysis of the power reflection coefficient is still under way.

Ishtar Terra forms the large block of uplifted terrain seen above roughly 60°N (near the top of Fig. 6). Within Ishtar Terra, Maxwell Mons, the highest elevation on the planet, reaches up to a radius of 6062 km (Fig. 7). At latitudes just below Ishtar in the upper center of the image lie the plains of Sedna (the deep-blue pool at 40°N); at 22°N, two prominent mountains, Sif (352°) and Gula (358°), reach to a radius of 6054.5 and 6055.5 km, respectively. Nearly centered in the image, and spanning the equator, is the large, 750-km-diameter corona ring called Heng-O; its rim rises about 0.5 km above the surrounding plains. Farther south, the heavily contorted Alpha Regio occupies a latitude band from 20°S to 30°S just east of the reference meridian. Deep in the south, centered on the reference meridian at 70°S is what appears to be a large circular shield, 1100 km in diameter, rising

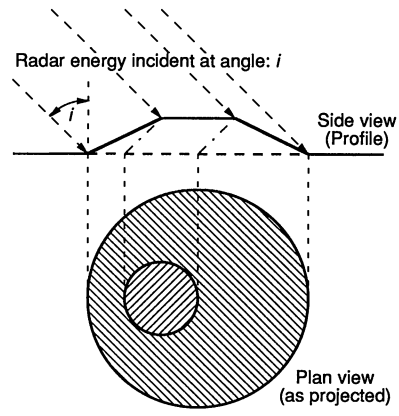

Fig. 5. The geometrical distortion associated with projecting a radar-imaged feature having finite relief on to a spherical surface of constant radius. The distortion depends both on the relief of the feature and the angle at which it is viewed.

to a radius of 6054.5 km, that is seen in its entirety for the first time by Magellan.

The thermal-emission radiometric mode is invoked for a part of the otherwise unused interval between the operation of the radar altimeter and the SAR in a given burst sequence (Fig. 2). In this mode, the radar system is connected on alternate bursts either to the HGA or to a terminating resistance, which protects the receiver while the transmitter is on but also provides a reference comparison at known temperature that assists in calibrating the receiver's gain as it drifts over time.

During radiometry, transmission is suppressed and the receiver monitors radio noise in the full 10-MHz bandwidth of the intermediate-frequency (IF) amplifier. In order to discriminate among input temperature variations of less than 2 K in a background of more than 1000 K, the (square-law detected) IF amplifier output is accumulated for 50 ms (to yield a time-bandwidth product of 5×10^5), and then sampled by a 12-binary-bit analog-to-digital converter. Tests made on the ground before launch suggest that the system can determine the antenna equivalent noise temperature, T_a, to an absolute accuracy of about 15 K, while discriminating fluctuations as small as 2 K over the short term.

In order to convert measurements of antenna temperature into an accurate estimate of the apparent brightness temperature, T_b, of the "scene" viewed from the spacecraft by the main lobe of the HGA, good knowledge of the complete HGA pattern is required. Direct measurements of the pattern were not possible before launch, for cost reasons, however. In particular, we need to know the ratio, ε, of T_a to T_b; ε is termed the beam efficiency (*12*) and typically is about 0.8 for antennas of this general design. The remainder of the antenna's sensitivity to its surroundings (the missing 0.2, less the inherent resistive or "copper" losses) comes primarily from the response of the antenna in all directions other than the main lobe, called the integrated sidelobe response.

Estimates of these quantities can be gleaned from measurements that were made during cruise, combined with dedicated calibrations that will be made shortly from Venus orbit. While the spacecraft was still distant from Venus during interplanetary cruise, the antenna temperature of the HGA was measured with its main beam and sidelobes observing mostly cold sky at a temperature near 3 K. Upcoming observations from orbit will measure the changing antenna temperature as the HGA is slewed from a normal radar mapping configuration into the local planetary zenith. These calibrations, together with a fairly accurate knowledge of the integrated disk brightness temperature, T_v, of Venus, derived from Earth-based observations over many years, should allow an estimate of the beam efficiency of the HGA. In the interim, we have assumed that ε has a value of 0.80.

During radiometric observations, the calculations also keep track of the solid angle occupied by the total disk of Venus, Ω_v, as viewed from the spacecraft, so that we may estimate and remove energy received in the HGA sidelobes. Thus, we find that

$$T_b \approx [T_a - T_v(1 - \varepsilon)\Omega_v/4\pi]/\varepsilon$$

where the small resistive losses in the HGA and contributions from the (3 K) cold sky have been neglected. Earth-based data (*6*) suggest that $T_v \approx 635$ K.

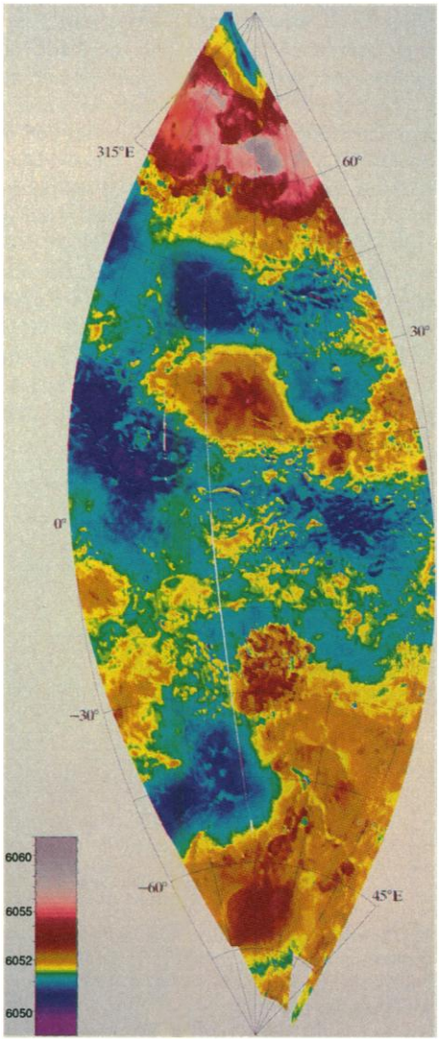

Fig. 6. False-color representation of Venus topography, as derived from the first 42 days (301 orbits) of radar operation. The relation between color and planetary radius is given in the scale at lower left. The map projection is transverse mercator, centered on the reference (0°) meridian, and spans approximately 60° of longitude. Lateral surface ("footprint") resolution varies with spacecraft altitude as shown in Table 4. Some small gaps in coverage, not exceeding about 20 km, have been smoothed over.

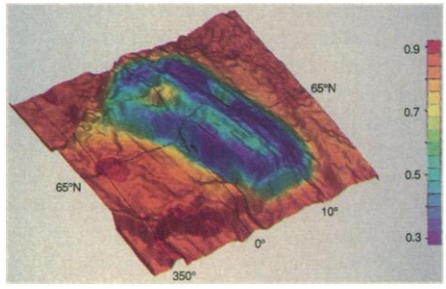

Fig. 7. False-color representation of the distribution of emissivity overlain on 3-dimensional shaded topography for the region surrounding Maxwell Mons. The relationship between color and emissivity is given in the scale at right. The highest part of the planet (rising to 6062 km) lies at approximately 65°N, 3°E. The depression at 66°N, 7°E, corresponds to Cleopatra Patera.

Having derived T_b for the scene as viewed from the spacecraft, we must next unravel the effects of the extensive Venus atmosphere. This layer transmits the energy emitted from the surface with a finite efficiency and replaces the loss with a temperature contribution of its own. (At the radar's wavelength of 12.6 cm, more than 87% of the energy emitted by the surface reaches the orbiting spacecraft.) We used an atmospheric radiation-transfer model derived for Magellan (*13*) to calculate both the (one-way) line-of-sight atmospheric transmission, α (as is also done to obtain the SAR radar cross section), and the atmospheric emission contribution, T'_{atm}. Both of these quantities are a function only of the incidence angle to, and altitude of, the observed surface, and may be calculated as a simple trigonometric correction to expressions given as polynomial expansions of that altitude for normal incidence.

These considerations lead to an expression for T_b that contains our desired end product, the surface emissivity, e, and allows its estimation

$$T_b = \alpha[e\,T_{surf} + \rho'(T'_{atm} + \alpha T_{sky})] + T'_{atm}$$

where T_{surf} is the physical temperature of the surface (also a function of altitude), ρ' is the surface Fresnel reflectivity, approximated in our analysis by $(1 - e)$, and T_{sky} is the brightness temperature of the reflected part of the celestial sky (above the atmosphere), usually taken as 3 K.

The task of estimating the physical surface temperature on Venus is made much easier than it would be on most other planets, because the thick CO_2-rich atmosphere acts as an efficient greenhouse blanket, holding in the heat energy contained in the surface

Table 5. Radiometer surface footprint resolution versus spacecraft altitude.

Spacecraft height (km)	Resolution	
	Along track (km)	Across track (km)
290	16	24
500	25	33
1000	44	50
2100	83	87

material and near-surface atmosphere. Thus, the temperature cannot change rapidly and is in adiabatic equilibrium; for a given elevation, the temperature is virtually the same everywhere: dark side to light side, pole to equator. Vertically, however, the temperature decreases at the adiabatic lapse rate of approximately -8 K km^{-1}. Thus, if we know the altitude of a surface region, we can immediately calculate its physical temperature, assuming it is in equilibrium with the overlying atmosphere (*14*). Because the Magellan altimetry experiment measures the height of the Venus surface, and does this with a lateral surface footprint resolution at least as small as that afforded to the emissivity determination by the 2° angular resolution of the HGA (Table 5), it is straightforward to calculate the actual physical temperature of the surface everywhere. The estimates of emissivity are included as entries in the ARCDR product, and are also resampled into a global emissivity image (GEDR), with 5-km pixels (Table 3).

A particularly interesting example of surface emissivity is from Maxwell Mons (Fig. 7). The area surrounding the Maxwell prominence is seen to be characterized by values of emissivity averaging about 0.85 (corresponding to a dielectric permittivity of 5), which are typical for the planet as a whole. At altitudes lying between 6055 and 6060 km radius, however, the emissivity drops rapidly to a low of 0.35, which requires a surface dielectric permittivity of 87. This general behavior has been noted before (*6*), but the resolution offered here allows a far more detailed look at the distribution of, and lower limits to, the values of emissivity in the Maxwell area. Interestingly, the northwest-southeast trending ridge to the left of the image center, where the altitude rises above 6060 to a maximum of 6062 km as noted earlier, shows emissivity increasing back to about 0.7. The reason for this apparent altitude dependence is not clear.

REFERENCES AND NOTES

1. The effective slant range, as also the along-track Doppler, resolutions given in Table 1 are determined as the half-power width of the response of the system to an echo from a point target (the point-spread, or ambiguity, function) and are approximately 0.4 times the inverse of the half-power width of the corresponding modulation transfer function. In the Magellan radar, the slant range resolution has been broadened, as compared to the theoretical value for the modulation bandwidth used, in order to reduce the variation in response against delay that would otherwise have been seen when sampling a point target echo at intervals of the reciprocal modulation bandwidth.
2. A detailed description of the radar system's operation is given by W. T. K. Johnson, *Proc. IEEE*, in press.
3. All of the MIDR products will become available to the general planetary and geological community through NASA's Space Science Data Center and its Planetary Data System, after they have been validated by the Magellan Project and scientific team.
4. T. Hagfors, *Radio Sci.* **5**, 189 (1970).
5. Figure 2 in J. W. Head *et al.*, *Science*, **252**, 276 (1991).
6. G. H. Pettengill, P. G. Ford, B. D. Chapman, *J. Geophys. Res.* **93**, 14,885 (1988).
7. Figure 16 in J. W. Head *et al.*, *Science* **252**, 276 (1991).
8. The pulse repetition rate (PRF) is fixed at 14,957 s^{-1} in the altimetric mode. Range aliasing (at delay multiples of 67 μs) within the antenna's illumination pattern becomes serious primarily at high altitudes, but even there it is important only for high values of positive or negative Doppler shifts along track, near the limits of the altimeter antenna response at an incidence angle of 5°. Doppler aliasing (at multiples of the PRF) is only important at low altitudes, where the spacecraft's orbital velocity is high. Rejection of data corresponding to highly Doppler-shifted surface footprints, which have incidence angles of more than a few degrees, relieves both problems.
9. In this approach, the mean received noise power, and its fluctuation in the absence of echo, are first estimated and used to establish a threshold. The position of the earliest significant echo power to exceed this threshold is then noted and reported as the surface height. No attempt has been made to refine the along-track dimension of the surface footprint through Doppler resolution.
10. See G. L. Tyler *et al.*, *Science* **252** 265 (1991).
11. At lower altitudes, the data are combined to broaden the effective along-track resolution to about 8 km in order to reduce statistical fluctuation ("speckle").
12. Note that beam efficiency is not the same thing as aperture effjciency, which is related to the point-source gain of the antenna and is known reasonably well, but which is not particularly helpful in interpreting filled-beam radiometry measurements.
13. Based on the Venus International Reference Atmosphere, issued by COSPAR, as vol. 5, No.11, of *Adv. Space Res.* (1985).
14. The mean thermal gradient down into the subsurface material is approximately 25 K km^{-1}, and the penetration of rdio waves through this near-surface material is likely not to exceed a few tens of meters; thus, with acceptable error, we can reasonably assume that the physical temperature for the emitting region is the same as for the surface and immediately overlying atmosphere.
15. D. O. Muhleman, *Astron. J.* **69**, 34, (1964).
16. We thank the entire Magellan Project staff for bringing the experimental techniques and measurements described here to successful fruition over many years of effort. Particular individuals who deserve mention are P. Graf, S. Lewicki, F. Liu, and J. Quigley.

10 January 1991; accepted 20 February 1991

Magellan: Electrical and Physical Properties of Venus' Surface

G. LEONARD TYLER, PETER G. FORD, DONALD B. CAMPBELL, CHARLES ELACHI, GORDON H. PETTENGILL, RICHARD A. SIMPSON

Magellan probes Venus' surface by 12.6-cm-wavelength vertical and oblique radar scattering and measures microwave thermal emission. Emissivity and root-mean-square slope maps between 330° and 30°E and 90°N and 80°S are dissimilar, although some local features are exceptions. Inferred surface emissivities typically are ~0.85, but vary from ~0.35 at Maxwell to ~0.95 northeast of Gula Mons and other locations. Lowest emissivities appear in topographically high areas; this relation suggests that a phase change or differences in chemical weathering occur at about 6055-kilometer radius. Initial results indicate that there are significant variations in the surface scattering function.

WITH THE EXCEPTION OF A SMALL number of locations examined by landing spacecraft (*1*), knowledge of the physical properties of Venus' surface must be inferred from observations of electromagnetic radiation either scattered or emitted by the surface. In the case of Magellan, interpretation is primarily from radar images and by classical geologic mapping techniques adapted for radar geometrical effects and large-scale scattering. Interpretation also involves determination of electromagnetic properties of the surface material and estimates of its physical structure from nonimaging data; these measurements serve as constraints and tests on geological hypotheses (*2–9*). In this report we describe, for the first 38 days (301 orbits) of Magellan operations, 12.6-cm-wavelength (λ) scattering and thermal-emission data and discuss possible inferences for Venus' surface properties. Our inferences apply to the statistical properties of the surface on wavelength-related scales but averaged over areas that at present are minimally of the order 100 km^2 (*10*).

Earlier observations were carried out at λ = 17 cm by the Pioneer Venus Orbiter,

G. L. Tyler and R. A. Simpson, Stanford University, Stanford, CA 94305.
P. G. Ford and G. H. Pettengill, Massachusetts Institute of Technology, Cambridge, MA 02139.
D. B. Campbell, Cornell University, Ithaca, NY 14853.
C. Elachi, Jet Propulsion Laboratory, Pasadena, CA 91109.